^{23}Na Nuclear Magnetic Resonance Study of $yNa_2S+(1-y)[xSiS_2+(1-x)PS_{5/2}]$ Glassy Solid Electrolytes

Ananda Shastri*[,1,2], Deborah Watson[†,3], Qing-Ping Ding[2], Yuji Furukawa[2,4], Steve W. Martin[2,3]

[1]Department of Physics and Astronomy, Minnesota State University Moorhead, Moorhead, MN 56560, USA

[2]Ames Laboratory, U.S. Department of Energy, Iowa State University, Ames, IA 50011, USA

[3]Department of Materials Science and Engineering, Iowa State University, Ames, IA 50011, USA

[4]Department of Physics and Astronomy, Iowa State University, Ames, IA 50011, USA

*Corresponding author: shastri@mnstate.edu, 218 477 2448

[†]Current address: 3M, Central Research and Development, St. Paul, MN

Abstract

^{23}Na NMR spin lattice relaxation times, T_1, and central linewidths were obtained for $yNa_2S+(1-y)[xSiS_2+(1-x)PS_{5/2}]$ glassy solid electrolytes for two series of glasses, y = 0.5 and 0.67, and x = 0.1, 0.3, 0.5, 0.7, and 0.9. No pronounced mixed glass former effect in the activation energy for T_1 relaxation was observed within experimental uncertainty for either series of glasses. DC Na^+ ion conductivity values calculated using NMR-derived correlation times, an available site coordination number z = 3 around the Na^+ ions, and an energy cutoff determined from the critical percolation threshold, were in agreement with the increasing trend in the experimental values for the y = 0.67 glasses. Using the same model, the conductivity values were calculated for the y = 0.50 glasses, which have as yet to be measured, and these revealed a decreasing conductivity as x increased. Energy barriers to sodium motion were calculated using the Anderson-Stuart model for the y = 0.67 sample, and the results suggested that the energy barriers as a function of composition are strongly influenced by the dielectric constant of these glasses. Sodium NMR second moment measurements show sodium-sodium separation distances decreasing by 6.5% across the full composition range of the glassy solid electolytes.

I. Introduction

Ionic conduction in glassy materials is of considerable scientific and technological interest [1]. In particular, sodium-based glasses have promise as solid-state electrolytes, and may result in lower cost batteries capable of high energy density, long cycle life, and safer operation. Given the ready availability of sodium in the oceans and in the earth's crust, rechargeable solid-state sodium batteries based upon fast sodium-ion conducting glassy solid electrolytes hold promise for providing low cost stationary storage of electric energy generated by solar and wind power [2-4].

In this investigation, we focus on the very promising ternary glass systems [5-11]. These glasses, represented as $yM_2X+(1-y)[xA+(1-x)B]$, consist of two glass network forming materials (A and B), and the network modifier component M_2X (M=Li, Na and X =O, S) added to give rise to ionic conduction. When the modifier is held constant with fixed mole fraction y, increasing x increases the concentration of glass former A while reducing that of B. The mixed glass former effect (MGFE) is observed when there is a non-linear, non-additive change in the physical properties observed across the glass system, x = 0 to x = 1. By mixing glass formers such as B_2O_3 and P_2O_5 with modifying alkali oxide such as Na_2O, significant nonlinear variations of physical properties (electrical, thermal, mechanical) are often found as a function of the mixed glass former composition, x (Ref. [8]). A positive MGFE occurs when these compositional changes improve the properties of the glass needed for conduction and has been seen in the $Na_2O + B_2O_3 + P_2O_5$ (NBPO) system [8,12]. A negative MGFE appears to be less common in these systems, but has been seen in the $Na_2O + SiO_2 + B_2O_3$ (NBSO) system [10]. The short-range order structures

formed and their connections to the physical properties as a function of the mixed glass former ratios are of considerable interest in understanding the origins of these positive and negative MGFEs. Therefore, in order to understand the origin, it is important to investigate the physical properties of the mixed glass former systems in detail.

Nuclear magnetic resonance (NMR) is a powerful experimental tool for extracting microscopic information at the individual nuclear sites within crystalline and amorphous materials [13-16]. The technique has been applied to many mixed glass former systems and has played a significant role in elucidating their microscopic physical characters. Considerable literature exists on the application of NMR to ionic conductors in general [16], and sodium-based glasses in particular [10,17,18]. The variation of the NMR spectrum with temperature can yield dynamic information about a specific nuclear isotope, and the nuclear relaxation times probe nuclear dynamics over frequencies ranging from tens of kHz to tens of MHz. Careful measurements and analysis of the mobile ion spin lattice relaxation time using low frequency NMR techniques can yield significant understanding of the conductivity controlling activation energies for cation jumping events in glasses, see for example references [10,16,19-25].

In previous NMR studies on Li-ion conducting glasses [22,23,26-28], the temperature dependence of the NMR spin-lattice relaxation time (T_1) and DC conductivities do not follow simple Arrhenius behavior. The first investigations were motivated by the need to explain non-Arrhenius behavior in NMR and conductivity data, as well as to account for discrepancies in the NMR- and conductivity-determined activation energies to ionic motion [23,26]. It was found that the non-Arrhenius behavior could be addressed

using two different methods: distributions of energy barriers [22,23,27] or non-exponential correlation functions. These authors found, however, that—all other factors being the same—using a distribution of activation energies (DAEs) was often preferable for several reasons [27]. First, it treated both the NMR and conductivity data within a single formalism. Second, it was naturally identified with the glassy state and third, it could be readily adapted to multiple-ion dynamics, where one population of ions exhibits markedly different dynamical behavior than another [28]. Further, discrepancies between NMR- and conductivity-derived energy distributions can be resolved by noting that while NMR should probe all ions—both mobile and immobile—conductivity detects only the mobile ones that generate a measurable current in response to the applied voltage, and hence samples a subset of the activation energies. For example, in many glassy solid electrolytes, lower activation energies have been reported for the DC conductivity data than the NMR data. This has been explained by a percolation model, in which ions in wells deeper than a percolation energy threshold cannot participate in long-range motion, but do participate in spin relaxation [22,23].

In sodium oxide glasses, ^{23}Na T_1 studies of the mobile Na^+ ion dynamics have focused on the considerably easier to prepare and handle, but significantly lower Na^+ ion conducting NBPO and NBSO oxide glasses [10]. The origins of the MGFE were probed with a variety of theoretical and experimental methods techniques. This work yielded significant insights into how the concentration of short range order structures in those systems with different Coulombic charges-trapping capabilities leads to the MGFE.

Though instructive, these oxide glassy solid electolytes have room temperature conductivities unsuitably low for energy storage applications, typically < 10^{-8} $(\Omega cm)^{-1}$ at 25 ^{o}C and far below benchmark values of 10^{-4} $(\Omega cm)^{-1}$ often thought required for application in solid-state batteries. One well-known option for improving the conductivity is to study the sulfide analogs of these systems. It was shown some time ago[29] that while a simple alkali oxide doped oxide glass such as $Na_2O + SiO_2$ has a room temperature conductivity of $\sim 10^{-9}$ $(\Omega cm)^{-1}$, the sulfide analogue $Na_2S + SiS_2$ can have a room temperature conductivity some 10,000-fold higher at $\sim 10^{-5}$ $(\Omega cm)^{-1}$. While still much lower than typical organic liquid electrolytes at 10^{-2} $(\Omega cm)^{-1}$, these conductivities make these sulfide glasses quite attractive and they are now the subject of a very active field of research. For these reasons, we have long studied the corresponding sulfide analogues of these common oxide glasses [7,9,19,28,30-35]. A unique challenge of studying these systems is that the highest ion conductivity is most commonly observed at the highest alkali sulfide content. Correspondingly, this is also at the lowest glass former content and likewise, typically, at the poorest glass forming ability. Hence, just as the glassy solid electrolyte becomes sufficiently conductive due to the increased alkali sulfide content, these compositions also require increasingly rapid cooling rates to reach the glassy state without the presence of (typically) conductivity lowering crystalline phases.

In our studies, we have observed however, that by mixing the glass formers in these systems the entropy of the liquid is significantly increased while presumably decreasing the liquidus temperatures through the formation of eutectics in the compositional phase field. These effects in turn create the observation that these glasses can be quite strongly

glass forming, requiring no more than free-cooling to reach the glassy state without the observable presence of any significant crystalline or polycrystalline phases. Among our many studies, this is the case of the system we report on here.

The macroscopic physical properties of $yNa_2S + (1-y)[xSiS_2+(1-x)PS_{5/2}]$ for the two series of glasses, y = 0.5 and 0.67, such as the distribution of short range order structures with composition x [36], ionic conductivity [37], glass transition temperature [36,37], molar volume [36,37], and density have been reported recently [36,37]. But, there is no report on these system yet of the dynamics of the Na^+ cations as measured by NMR. In this paper, we have carried out ^{23}Na NMR measurements, for two series of glasses, y = 0.5 and 0.67, with x = 0.1, 0.3, 0.5, 0.7, and 0.9 to investigate the Na^+ ion dynamics from a microscopic point of view. We have kept the number of glass formers constant in this system by using $PS_{5/2}$ instead of the more common P_2S_5 [30].

Based on NMR data, the DAEs as a function of composition were determined. In addition, DC conductivity values were calculated using NMR-derived correlation times and percolation theory, and were compared with available experimental values for y = 0.67. From this, a Na^+ ion dynamics model was created to predict DC conductivities for the as yet unmeasured y = 0.50 system, where rapid crystallization on cooling has frustrated the formation of amorphous samples large enough for conductivity measurements. Further, energy barriers were analyzed using the Anderson-Stuart model [30,38], and the dependence on key parameters investigated. Finally, sodium ion clustering was investigated by NMR second moment measurements as a function of sample composition.

II. Experimental Methods

Glassy solid electrolytes for y = 0.50 and 0.67 and x = 0.1, 0.3, 0.5, and 0.9 were prepared as described elsewhere [36,37,39]. Powder XRD and SEM EDS compositional analyses wereperformed on representative samples in this series, and it was found that all samples tested were X-ray amorphous and their compositions were as batched to within a few percent. Samples for NMR were flame sealed in thin-walled quartz tubes under 0.16 atm of helium gas.

The main challenge in this work was to extract motional information about the sodium ion by changing temperature over a wide enough range to probe sufficient change in the correlation times, but without exceeding the glass transition temperature, T_g, and thus altering the structure of the glass [10].

NMR measurements were performed on ^{23}Na (nuclear spin I=3/2, gyromagnetic ratio $\gamma/2\pi$=11.2653 MHz/T) by using a homemade phase-coherent spin-echo pulse spectrometer from 4.2 K to just below the T_g of the samples, ~500 K. The ^{23}Na NMR spectra were obtained either by sweeping the external magnetic field B_0 at a fixed Larmor frequency of $\nu_L = 83.45$ MHz or by Fourier transform of the NMR echo signals at a constant magnetic field of B_0 =7.41 T. The ^{23}Na spin-lattice relaxation rates, $R_1 = 1/T_1$, were measured by the saturation recovery method [40]. The ^{23}Na rigid-lattice second moment M_2 due to the magnetic dipole-dipole interaction, was obtained following the methods described in Refs. [18,41]. Following this method, spin-echo measurements were performed using the Hahn spin echo sequence ($\frac{\pi}{2}\Big|_x - \tau - \pi_y - \tau - echo$), taking care to irradiate only the central line. The duration of the $\pi_y$pulse was 10-14 μs. As will be shown

in the next section, because we found that detectable sodium ionic motion ceased for all samples at 150 K and below, a temperature of 100 K was deemed suitable for all subsequent rigid lattice M_2 measurements.

III. Results

A. ^{23}Na NMR spectrum

The typical spectrum for a nucleus with spin I=3/2 with Zeeman and quadrupolar interactions can be described by a nuclear spin Hamiltonian [13,14]

$$\mathcal{H} = \mathcal{H}_Z + \mathcal{H}_Q + \mathcal{H}_D \tag{1}$$

where $\mathcal{H}_Z = -\gamma\hbar B_0 I_z$ is the interaction of the nuclear spin with the external magnetic field B_0, $\mathcal{H}_Q = \frac{e^2qQ}{4I(2I-1)}[(3I_z^2 - I^2) + (\frac{\eta}{2})(I_+^2 + I_-^2)]$ is the electric quadrupole interaction, and $\mathcal{H}_D$ is the magnetic dipole-dipole interaction between nuclear spins. $\mathcal{H}_Q$ is written in principal axis system (PAS) of the electric field gradient $V_{ij.}$ The PAS axes are defined such that $|V_{ZZ}| \geq |V_{YY}| \geq |V_{XX}|$. Here eQ is the quadrupole moment of the ^{23}Na nucleus, $eq = |V_{ZZ}|$, the quadrupole frequency $\nu_Q = \frac{3e^2qQ}{2I(2I-1)h}$, and asymmetry parameter $\eta = \frac{V_{XX} - V_{YY}}{V_{ZZ}}$.

When the Zeeman interaction is greater than the quadrupolar interaction, this Hamiltonian produces a spectrum with a sharp central transition line (I_z=-1/2↔ 1/2) flanked by one satellite peak on either side (I_z=1/2↔ 3/2 and -1/2↔ -3/2). Since the samples are in the form of a powder, the spectrum is an NMR powder pattern [42]. Figure

1 shows the typical ^{23}Na spectrum for the satellite lines observed at 4.2 K in the y = 0.67 and x = 0.1 powder sample.

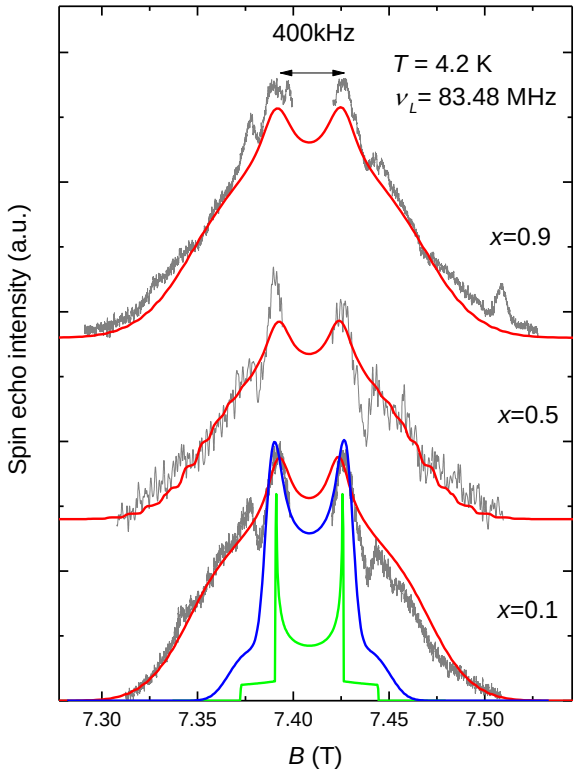

FIGURE 1. Field swept ^{23}Na spectra for $0.67Na_2S+0.33[xSiS_2+(1-x)PS_{5/2}]$ glasses x = 0.1, 0.5, and 0.9. Measurements (represented as gray lines) were performed at T=4.2 K and ν_L =83.48 MHz. Due to the narrowness of the central line compared to that of the satellite peaks, the field sweep was not performed over the central line region. Red solid lines are simulations of the first order electric quadrupole powder patterns as described in the text for a Gaussian distribution of parameters ν_Q and η. Results are listed in Table 1. The green curve shows a simulation of powder pattern with a fixed ν_Q and a fixed η = 0 without any distributions. The blue curve represents a simulated powder pattern with a Gaussian distribution in ν_Q and no distribution in η.

The observed satellite lines are too broad to be explained by a single value of ν_Q and η as shown in Fig. 1, where the green curve represents a simulated powder pattern $f(\nu_Q,\eta)$

for ν_Q = 0.4 MHz and η = 0, using the well-known quadrupolar powder pattern line shape given in [42]. A powder pattern described by a single ν_Q and η would suggest a well defined local environment for the Na, as would be expected for a crystalline powder, but distributions of these quantities would be expected for amorphous samples [16]. One may model distributions in the local environments by creating a weighted sum of powder patterns $\sum_{\nu_Q}\sum_{\eta} g_1(\nu_Q)g_2(\eta)\,f(\nu_Q,\eta)$, where $g_1(\nu_Q)$ and $g_2(\eta)$ are distributions of ν_Q and η. Using only a distribution in ν_Q does not suffice, as seen by the blue curve in Fig. 1, where a Gaussian distribution with mean ν_Q = 0.4 and standard deviation σ_{ν_Q} = 0.2 MHz was used, with η = 0. In order to reproduce the broad satellite line, it is necessary to use two independent Gaussian distributions in ν_Q and η, with ν_Q = 0.9 MHz, σ_{ν_Q} = 0.2 MHz, η = 0.2 and σ_η = 0.1, as shown at the bottom of Fig. 1 by the red curve. These results indicate that the local atomic-level environment around the Na^+ ions are highly inhomogeneous in these glass compositions.

Similar broad satellite lines are observed in all mixed glass former compounds with y = 0.67 studied here. The typical spectra observed for three of the five samples across the compositional range of the system studied (x = 0.1, 0.5, and 0.9) are shown in Fig. 1, together with the simulated spectra whose fitting parameters are summarized in Table 1. As shown in Table 1, distributions of ν_Q and η are not significantly different across the glass series.

Sample	ν_Q (MHz) mean±SD	η mean±SD
x=0.1	0.9±0.2	0.2±0.1
x=0.5	0.9±0.2	0.3±0.1
x=0.9	0.9±0.2	0.28±0.09

Table 1. ^{23}Na electric quadrupole parameters ν_Q and η for $0.67Na_2S+0.33[xSiS_2+(1-x)PS_{5/2}]$ glasses obtained from the simulated powder patterns of Fig. 1 as described in the text. A Gaussian distribution of both ν_Q and η was assumed, and is given in the table as the mean ± standard deviation.

Similar, but slightly broader, ^{23}Na NMR satellite lines have also been observed in the y = 0.50 series, as shown in Fig. 2 where the spectrum for x = 0.1 glass measured at 4.2 K is shown as an example. The broadening due to the distributions results in an indistinct quadrupole shoulder, making it difficult to find unique parameter values. However, the values ν_Q = (1.1 ± 0.3) MHz η =(0.3 ± 0.1) reasonably reproduced the observed spectrum as shown by the black curve, indicating that the values of ν_Q and η are not significantly different from those for the y = 0.67 samples. For simplicity, then, we took the values for the two systems y = 0.50 and y = 0.67 to be the same: ν_Q = (0.9 ± 0.2) MHz and η = 0.3 ± 0.1.

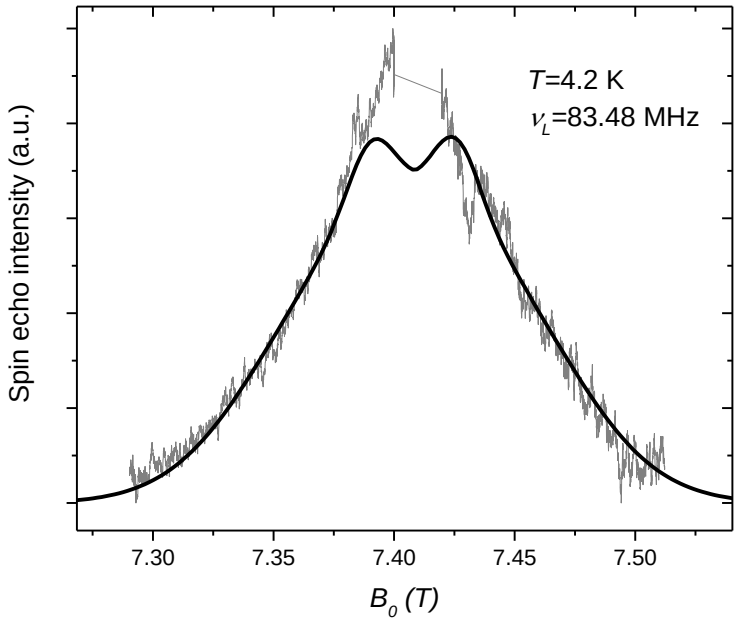

FIGURE 2. Field-swept ^{23}Na spin-echo amplitude versus magnetic field scans for $0.50Na_2S+0.50[xSiS_2+(1-x)PS_{5/2}]$ glass x = 0.1. Due to the narrowness of the central line compared to that of the satellite peaks, the field sweep was not performed over the central line region. Solid lines are simulations of the first order electric quadrupole powder patterns as described in the text for a Gaussian distribution of parameters ν_Q and η. Lack of a clear quadrupole shoulder complicated the determination of the fit parameters. The simulation shown here is for $\nu_Q = (1.1 \pm 0.3)$ MHz and $\eta = 0.3 \pm 0.1$.

Figure 3 shows the ^{23}Na NMR central line obtained from the Fourier transform of the half spin-echo NMR signal, for the y=0.67, x = 0.1 glass at different temperatures. As can be seen, the full-width at half maximum (FWHM) of the central line depends on temperature. The FWHM is nearly constant at low temperature, then starts to decrease around 150 - 200 K with increasing temperature and then levels off at higher temperatures, as summarized in Fig. 4(a) for all y = 0.67 series samples studied here.

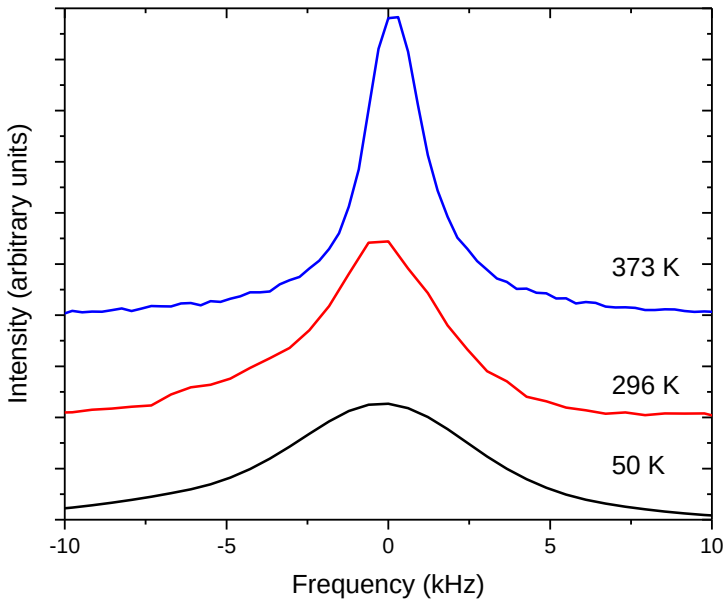

FIGURE 3. Typical temperature dependence of ^{23}Na NMR central lines for $0.67Na_2S+0.33[xSiS_2+(1-x)PS_{5/2}]$ glass for x=0.1. The figure illustrates the motional narrowing of the NMR line with increasing temperature.

The temperature dependence of the FWHM provides information about the time scale of nuclear motion. The temperature independent behavior at low temperatures is due to the freezing of the ionic motion, and the reduction in the FWHM occurs when the fluctuation frequency of the local field approaches the rigid-lattice central line width, on the order of 10 kHz. With further increase in the frequency, the NMR central line is completely narrowed, giving rise to a lower constant value of FWHM observed at higher temperature.

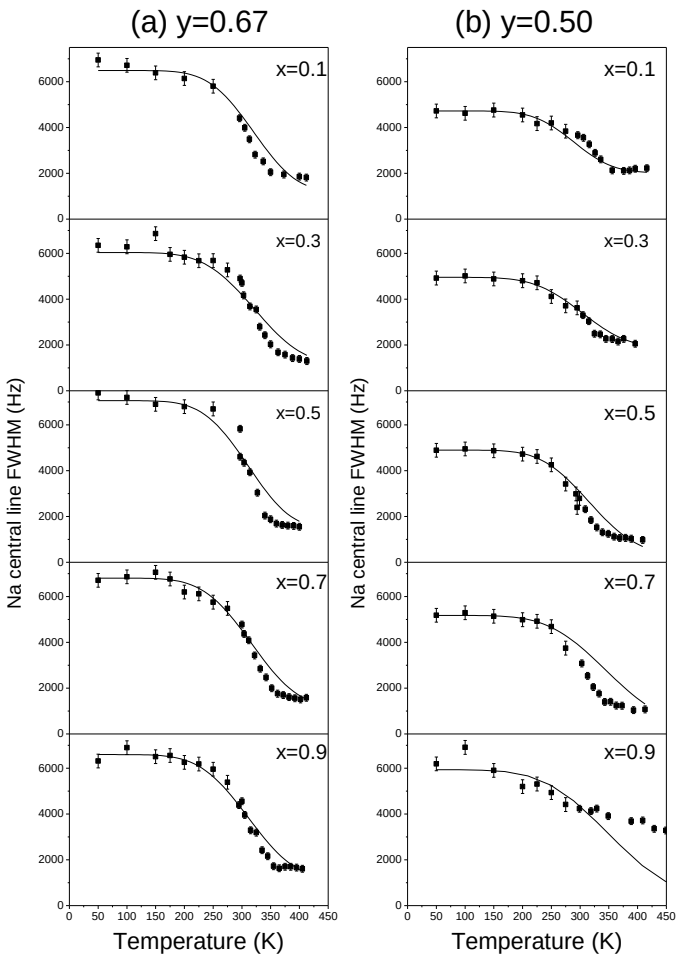

FIGURE 4. Temperature dependence of FWHM for the ^{23}Na NMR central line for $yNa_2S+(1-y)[xSiS_2+(1-x)PS_{5/2}]$ glassy solid electrolytes for two series of glasses with x = 0.1, 0.3, 0.5, 0.7, and 0.9. (a) y = 0.67. (b) y = 0.5. The solid lines were determined by simultaneously fitting line width and R_1 data as described in the text assuming a Gaussian distribution of activation barriers.

In the case of the y = 0.5 series samples, similar temperature dependence of the FWHM is observed as shown in Fig. 4(b). However, the raw FWHM line widths increased as temperature decreased, indicating the presence of a paramagnetic impurity. Such

increases of FWHM at low temperature were not observed in the y = 0.67 series of samples. The effect was eliminated by fitting raw FWHM line widths in the temperature range below where motional effects become appreciable, 50-150 K, to a Curie model y = A+B/T. The paramagnetic contribution B/T was then subtracted from the raw FWHM at all temperatures. These values are given in Table 2, and a discussion of the contribution this makes to nuclear relaxation is given in Section V. We believe the paramagnetic impurity to be Fe which arises from the steel container used to mill the samples to a fine powder required for the NMR measurements. We are repeating some of these measurements using samples prepared in ceramic containers to investigate this hypothesis.

x	B (Hz K)	H_{loc} (T) at 300 K	R_{1pmax} (s^{-1})
0.1	2.6×10^4	5.1×10^{-6}	0.000765
0.3	2.5×10^5	5.0×10^{-5}	0.074156
0.5	5.1×10^4	1.0×10^{-5}	0.003013
0.7	3.6×10^4	7.1×10^{-6}	0.001497
0.9	1.6×10^5	3.2×10^{-5}	0.031407

Table 2. ^{23}Na central line FWHM paramagnetic contribution parameter B for $0.50Na_2S+0.50[xSiS_2+(1-x)PS_{5/2}]$ glasses. The estimated local field H_L due to the paramagnetic ion, and the estimated maximum contribution to the nuclear spin-lattice relaxation R_1 are described in Section V.

B. ^{23}Na spin-lattice relaxation

Further information about the time scale of nuclear motion may be obtained from temperature dependence of the spin-lattice relaxation rate, $R_1 \equiv 1/T_1$. The nuclear spin-lattice relaxation time T_1 of the ^{23}Na central transition (-½↔ ½) were obtained by the saturation recovery method [40]. In crystalline materials for nucleus with I = 3/2, this selective irradiation of the central line combined with a well-defined transition probability resulting from the time-dependent interaction as the nucleus hops through the lattice produces a double-exponential behavior [43]. However, in glassy materials a broad distribution of nuclear interactions results in a distribution of nuclear relaxation times, and may be modeled by a stretched exponential function. The normalized longitudinal magnetization $1 - M_z(t)/M_\infty$ was fit to a stretched exponential function [1,10]

$$1 - M_z(t)/M_\infty = \exp\left[-\left(\frac{t}{T_1}\right)^{\beta}\right] \qquad (2)$$

The quantity β characterizes the distribution of interaction strengths throughout the sample. Single relaxation time behavior is recovered in T_1 for β = 1. We initially performed the fits using Eqn. (2) and allowed both β and T_1 to be adjustable parameters. We chose to average β for all temperatures, and then refit the data with β fixed at the average value over all temperature for each sample. This method inherently assumes that any temperature dependence of β over the temperature range studied is small. We have studied other

systems, Li glasses in particular, where β is strongly temperature dependent and the simplification used here is not valid [27].

Figure 5 shows the normalized longitudinal magnetization of the ^{23}Na central line versus time between saturation and the read pulse for the x = 0.1 sample at several temperatures.

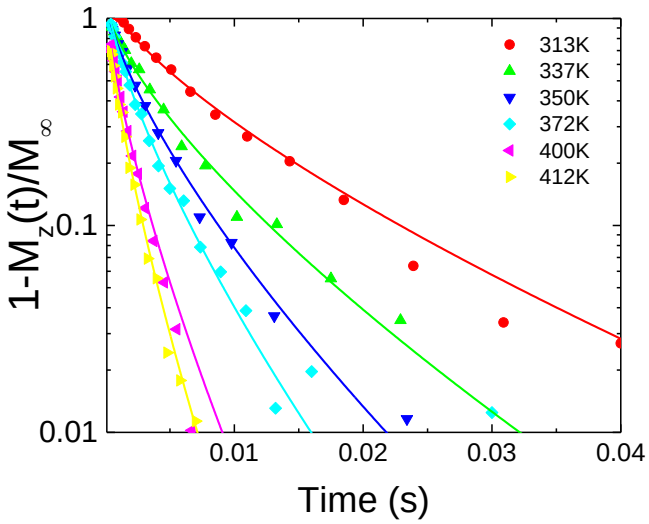

FIGURE 5. Example spin-lattice relaxation data of the ^{23}Na central line for $0.67Na_2S+0.33[xSiS_2+(1-x)PS_{5/2}]$ glasses, where x = 0.1. The method for estimating the stretched exponential parameter β over the temperature range studied is described in the text. For this sample, $\beta = 0.82 \pm 0.02$, and the fits using this value are shown as solid lines.

Solid lines represent fits to Eqn. (2) with β fixed to the average value given in Fig. 6 for each sample.

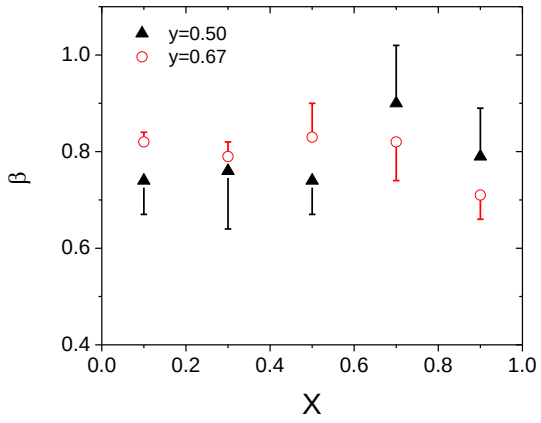

FIGURE 6. Stretched exponential parameter β determined from the ^{23}Na central lines nuclear spin-lattice relaxation of $yNa_2S+(1-y)[xSiS_2+(1-x)PS_{5/2}]$ glasses for y = 0.50, 0.67 and x = 0.1, 0.3, 0.5, 0.7, and 0.9. These values were extracted from the magnetization recovery data (Fig. 5), and described in the text. Error bars are symmetric, but only one side was drawn for each data point to simplify the graph.

The estimated R_1 values versus 1000/T are plotted in Figs. 7(a) and 7(b). Theory predicts that R_1 becomes a maximum at the temperature where the inverse correlation time for nuclear motion $1/\tau$ is on the order of the Larmor frequency, ω_L.

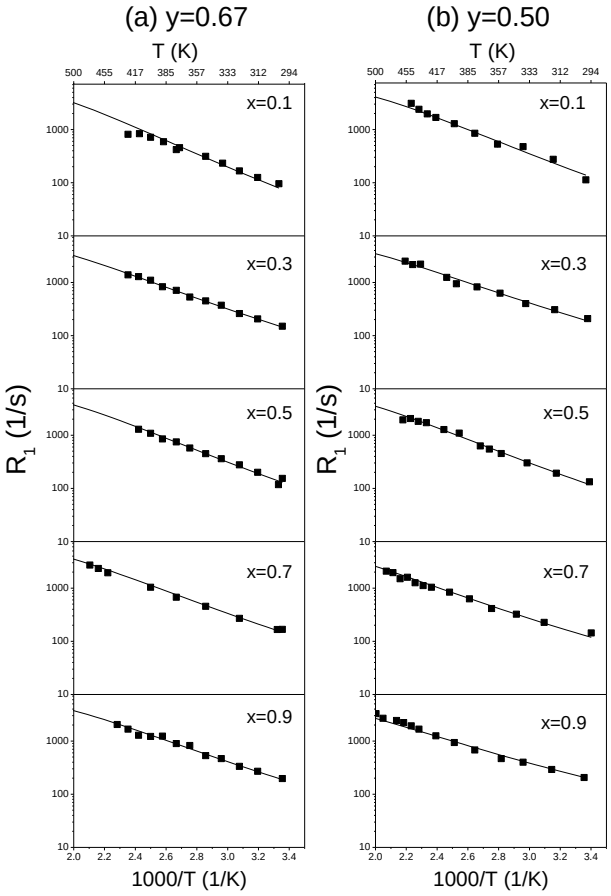

FIGURE 7. Temperature dependence of ^{23}Na spin-lattice relaxation rate R_1 for $yNa_2S+(1-y)[xSiS_2+(1-x)PS_{5/2}]$ glassy solid electrolytes for two series of glasses with x = 0.1, 0.3, 0.5, 0.7, and 0.9. (a) y = 0.67. (b) y = 0.5. The solid lines were determined by simultaneously fitting line width and R_1 data as described in the text assuming a Gaussian distribution of activation barriers. Error bars are within the size of the marker.

As seen in Fig. 7, the maximum in R_1—expected for cross-over from slow-motion to a fast-motion regime—could not be observed experimentally. This is due to the relatively low T_g for all of these samples. The low T_g values of these glasses are consistent with the presumed low liquidus (T_L) temperatures for these compositions. $T_L \sim (3/2)T_g$ is observed

for nearly all glass forming liquids [44]. Thus, data are in the slow motion (frequency dependent) regime for nuclear motion.

C. ^{23}Na second moment

The rigid-lattice second moment M_2, measured for experimental conditions in which the ionic motion is frozen out, and in which the dominant interaction between nuclei is the magnetic dipole-dipole interaction, was calculated by Van Vleck [14]. For quadrupolar nuclei such as ^{23}Na in glasses, modifications must be made. The key ideas are as follows. The fluctuation of precession rates due to local field variations tend to reduce the spin-echo amplitude. Homonuclear magnetic dipole-dipole and electric quadrupole interactions, which are bilinear in I_z, are not refocused by the NMR pulse sequence, and lead to a reduction in spin-echo amplitude [41]. By applying π pulses selectively to the central transition (I_z=-1/2↔ ½) for quadrupolar nuclei, the system can be made to act like a spin ½ system, and the spin-echo decay spectroscopy yields information specifically about the magnetic dipole coupling [45]. The criterion for selective irradiation of the central line is $\left|\mathcal{H}_Q^{(1)}\right| >> \left|\mathcal{H}_{rf}\right| >> \left|\mathcal{H}_Q^{(2)}\right|, \left|\mathcal{H}_D\right|$, where $\left|\mathcal{H}_Q^{(1)}\right|$ and $\left|\mathcal{H}_Q^{(2)}\right|$ are the magnitudes of the first and second order quadrupole contributions to the Hamiltonian, $\left|\mathcal{H}_{rf}\right|$ is the magnitude of the radio frequency π pulse used to flip the spins, and $\left|\mathcal{H}_D\right|$ is the nuclear magnetic dipole-dipole contribution. For these experiments, $\left|\mathcal{H}_Q^{(1)}\right|$ □ 1 MHz (Table 1) and $\left|\mathcal{H}_Q^{(2)}\right|, \left|\mathcal{H}_D\right|$ □ 8 kHz (Fig. 4). The π pulse durations were $\tau_\pi = 10\text{-}14$ μs, resulting in a spectral width of approximately $1/\tau_\pi$ □ 70 kHz, thus fulfilling the selective irradiation criterion. Further, due to a distribution of second moment values arising in many sodium compounds, it has been

shown that the ^{23}Na second moment M_2 determined in the limit of short evolution times yields experimental values consistent with theoretical ones where crystalline structure is known [18,41].

Figure 8 illustrates the method. The normalized spin-echo amplitude $\frac{I(2\tau)}{I_0}$ versus evolutions time 2τ is shown, and was fit to

$$\frac{I(2\tau)}{I_0} = exp\left(-\frac{M_2}{2}(2\tau)^2\right) \tag{3}$$

for evolution times up to $2\tau_{max}$.

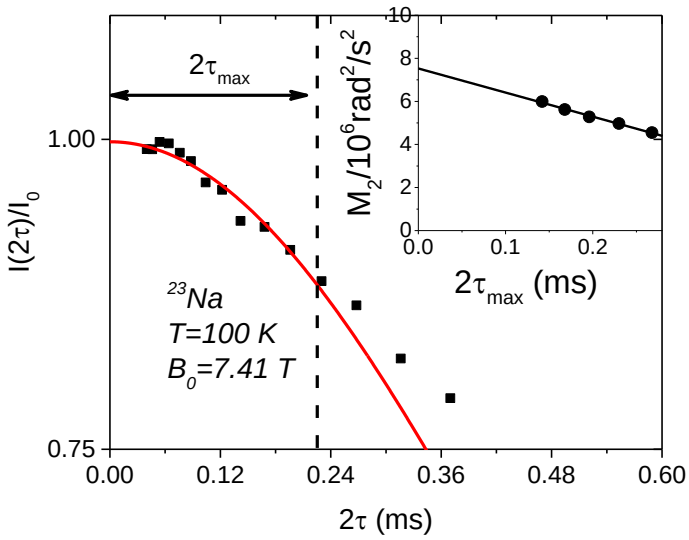

FIGURE 8. Method for determining ^{23}Na central line second moment in the limit of short evolution times, illustrated for the $0.67Na_2S+0.33[xSiS_2+(1-x)PS_{5/2}]$ glass x=0.1. The normalized spin-echo amplitude versus evolutions time 2τ. is shown in the outer graph. The solid line shows a fit to the Gaussian curve $\frac{I(2\tau)}{I_0} = exp\left(-\frac{M_2}{2}(2\tau)^2\right)$ from time 0 up to $2\tau_{max}$ (dotted line). M_2 was plotted as a function of $2\tau_{max}$ (inset). A linear fit determined M_2 in the limit of zero evolution time. In this case, $M_2=(7.5\pm 0.1)\times 10^6 rad^2/s^2$.

From this, M_2 was determined as a function of $2\tau_{max}$. As shown in the Fig. 8 inset, by extrapolating to time 0, the M_2 in the limit of short evolution times was determined. It is related to the Na-Na distances r_{ij} by [18,41,45]

$$M_2 = 0.9562\left(\frac{\mu_0}{4\pi}\right)^2 \gamma^4 \hbar^2 \sum_i r_{ij}^{-6} \tag{4}$$

V. Discussion

A. ^{23}Na motional activation energies

The activation energies for ^{23}Na motion may be obtained by performing simultaneous fits to both the line width, FWHM, and relaxation rates, R_1 (Ref.[10]). In this treatment, the correlation time for nuclear motion was assumed to follow the Arrhenius law

$$\tau(T) = \tau_\infty \exp\left(\frac{\Delta E_{act}}{k_B T}\right) \tag{5}$$

where ΔE_{act} is the activation energy for nuclear motion, and τ_∞ the correlation time at infinite temperature. Following Ref. [10], τ_∞ was fixed at 10^{-13} s for all calculations. In our many studies of these systems, we have observed that due to the disordered nature of the short range order in these glasses, the energy environments around the mobile cations are distributed and this leads to a DAEs for ion hopping events in these glasses [21,22]. A

Gaussian distribution of activation energies has provided a good description of this distribution and is used here. It is given by

$$g(\Delta E) = \frac{1}{\sigma_E \sqrt{2\pi}} \exp\left(-\frac{(\Delta E - \Delta E_{act})^2}{2\sigma_E^2} \right) \tag{6}$$

In the analysis, and consistent with our previous studies, both the mean barrier height for nuclear motion ΔE_{act} and the standard deviation of the energy barrier distribution σ_E were taken to be the only free-fit parameters. The central line width as a function of temperature was modelled using the relation [10,13]

$$\delta\omega^2 = \int_0^\infty d\Delta E \;\; g(\Delta E) \left[\delta\omega_\infty^2 + \frac{2}{\pi} \left(\delta\omega_0^2 - \delta\omega_\infty^2 \right) \times \tan^{-1}\left(\tau(\Delta E) \cdot \sqrt{\delta\omega^2} \right) \right] \tag{7}$$

Here $\delta\omega_0^2$ and $\delta\omega_\infty^2$ represent the low- and high-temperature values of the second moment of the line width. Assuming the dominant interaction is the fluctuating nuclear quadrupole interaction as the sodium hops through the glass, and assuming exponential correlation times, theory gives the relaxation rate for the central line to be [10]

$$R_1 \equiv \frac{1}{T_1} = \frac{4\pi^2 \nu_Q^2}{5} \left(1 + \frac{\eta^2}{3} \right) \int_0^\infty d\Delta E \;\; g(\Delta E) \left[\frac{\tau}{1 + (\tau\omega_L)^2} + \frac{\tau}{1 + (2\tau\omega_L)^2} \right] \tag{8}$$

Note that the formula in Eq. (7) introduces no new fit parameters, since ν_Q and η are already known. Using Eqns. (5-8) and the ν_Q and η values of Table 1, for each sample simultaneous fits of the central line width and $1/T_1$ data were performed, and are shown as solid lines in Figs. 4 and 7.

Several points may be noted. First, measurements reveal that $\nu_L \approx \nu_Q \approx FWHM$ consistent, and the dominant interaction is the nuclear quadrupole, consistent with the original assumptions. For the y = 0.67 series of glasses, the model appears to adequately describe both the FWHM and R_1. The fit appears to be less good for the y = 0.50 series of glasses, and, in particular, the x = 0.9 sample does not yield a fully narrowed ^{23}Na line up to T_g. We are continuing to investigate the source of this discrepancy. The paramagnetic effects were subtracted out of the FWHM data and do not contribute to the R_1 significantly at high temperatures. This was verified by estimating the contribution to the relaxation rate from magnetic impurities. The line broadening occurs due to a distribution of line shifts from the interaction between the local field H_L due to the paramagnetic ion and the magnetic dipole moment of ^{23}Na. This contribution to the line width and its connection to the Curie paramagnetic fit parameter B may be expressed as $\mu H_{loc} = \frac{hB}{T}$, where μ is the ^{23}Na nuclear magnetic dipole moment, h is Planck's constant, and T is the Kelvin temperature. From this $H_{loc} = \frac{hB}{\mu T}$ was determined for T=300 K, and is listed in Table 2. The paramagnetic contribution to relaxation for dilute impurity concentrations has been described by $R_{1p} = \gamma^2 \left\langle H_{loc}^2 \right\rangle \frac{\tau_e}{1+\left(\omega_L \tau_e\right)^2}$ [13,46-48] where τ_e is the electronic correlation time arising from the paramagnetic impurity, and ω_L is the nuclear Larmor frequency. The electronic correlation time is described by an Arrhenius relation with its own activation energy, describing the tendency for molecular reorientation of the impurity ion [47]. The maximum ^{23}Na paramagnetic relaxation rate becomes $R_{1p\max} = \frac{\gamma^2 \left\langle H_{loc}^2 \right\rangle}{2\omega_L}$ and when

evaluated for T=300 K is expected to give an upper limit on the relaxation rate due to the paramagnetic impurity. From Table 2 the $R_{1p\max}$ values for the y=0.50 samples are typically three orders of magnitude smaller than the measured R_1 values at 300 K in Fig. 7(b). We take this as a further indication that the dominant relaxation mechanism over the temperature range we probed is quadrupole relaxation, and at these temperatures ignoring the contribution from paramagnetic impurities is justied. Second, we noted that assuming a distribution of activation energies was important to obtaining simultaneous fits to FWHM and R_1 data. Without this assumption, adequate fits could not be obtained. The average barrier heights ΔE_{act} for the Gaussian distribution for all compositions studied are summarized in Fig. 9.

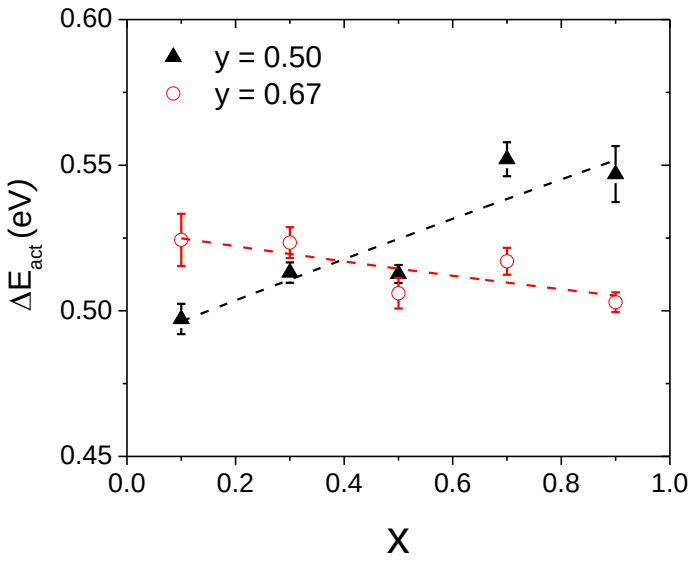

FIGURE 9. ^{23}Na average barrier energy ΔE^*_{act} determined by NMR for $yNa_2S+(1-y)[xSiS_2+(1-x)PS_{5/2}]$ glasses for y=0.50, 0.67 and x =0.1, 0.3, 0.5, 0.7, and 0.9. The values are the mean values obtained from Gaussian distributions determined from fits using NMR data in Figs. 4 and 7 and the method described in the text. The error bars represent the uncertainty in the mean value determined from the fit. The standard deviation of the Gaussian distributions is not shown, but was σ_E 0.10 eV. The dotted lines are guides for the eye.

The distribution widths as measured by the standard deviation σ_E were all within the range (0.10±0.01) eV. Third, we tested other values of τ_∞, specifically $\tau_\infty = 10^{-14}$ s, but this resulted in fits that deviated significantly from both datasets, and was rejected. Lastly, we checked that the resulting values from the Arrhenius model and the ΔE_{act} values gave plausible correlation times. The method of Bjokstam et al. [10,49] gives a correlation time estimate of $\tau_{1/2} \approx 0.3/\delta\nu_{1/2}$ at the temperature where the line-width is $\delta\nu_{1/2} = (\delta\nu_0 + \delta\nu_\infty)/2$. This resulted in $\tau_{1/2} \approx 80\mu s$ at 300 K for the x = 0.1 sample, which is on the same order of magnitude as the 50 μs at 300 K from the Arrhenius model obtained from Eqn. (5) using the value of ΔE_{act} for the x = 0.1 sample. Finally, the anomalous behavior of the y=0.50, x=0.9 may be an indication that one or both of the assumptions regarding the DAE and the nature of the relaxation mechanism are violated. Since the fit to the FWHM data appears to underestimate the ΔE_{act}, it is possible that this is in fact somewhat higher. This would accentuate the trend indicated in Fig. 9. However, further work is needed to settle this quesiont. Overall, general agreement between the model and data are consistent with the dominant ^{23}Na relaxation mechanism being the quadrupole interaction, a Gaussian distribution of activation energies, and $\tau_\infty = 10^{-13}$ s for nearly all samples studied.

B. Anderson-Stuart model for ΔE_{act}

ΔE_{act} values estimated from the FWHM and R_1 data are shown in shown Fig. 9. ΔE_{act} shows clear changes as the SiS_2 concentration x increases, although the changes are not significant. For the y = 0.50 series, the activation energy increases, and for y = 0.67 it

decreases. The dotted lines are unweighted parabolic fits to the data. These curves appear very nearly linear, suggesting the MGFE is relatively weak in these systems.

In order to discuss the compositional dependence of ΔE_{act} in more detail, we adopt the Anderson-Stuart model [30,38]. According to this model, the activation energy is the sum of a Coulombic contribution, ΔE_C, arising from the electric interactions between the mobile cation and the other ions in the glass, and a strain contribution, ΔE_S, arising from the lattice strain caused by the cations displacing the other network ions in the glass as they move through the structure. The total activation energy is then:

$$\Delta E_{act} = \Delta E_C + \Delta E_S \tag{9}$$

Parameters necessary for calculating the Coulombic contribution to the activation energy are indicated in Fig. 10.

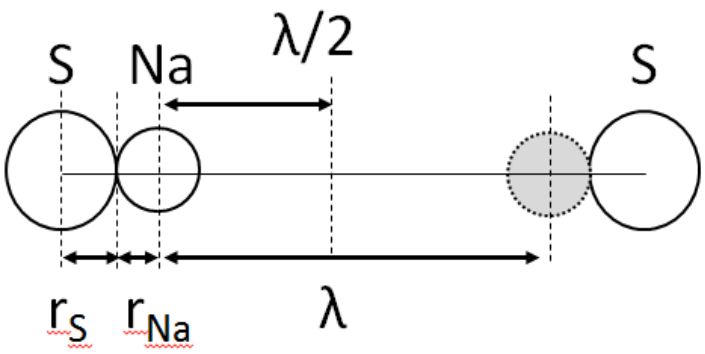

FIGURE 10. Diagram of relevant quantities needed for estimating the Coulombic contribution in the Anderson-Stuart model. The sodium and sulfur ionic radii are indicated, as well as the average jump distance λ from one sodium site to another. The shaded circle indicates an unoccupied sodium site to which the sodium cation can jump.

The Coulombic contribution is defined as the energy difference between the sulfur-sodium interaction at ion separations of $r_S + r_{Na}$ and $r_S + r_{Na} + \lambda/2$ yielding [30]:

$$\Delta E_C = \frac{kZ_{Na}Z_S e^2}{\varepsilon_\infty}\left(\frac{1}{r_S + r_{Na}} - \frac{1}{r_S + r_{Na} + \lambda/2}\right) \tag{10}$$

where k = Coulomb's constant, Z_{Na} = sodium charge, Z_S = sulfur charge, r_{Na} = sodium radius, r_S = sulfur radius, λ = sodium cation separation, ε_∞ = dielectric constant.

The average sodium-sodium distance λ may be estimated from the molar volume V_m using a simple cubic model by

$$\lambda = \sqrt[3]{\frac{V_m/2y}{N_A}} \tag{11}$$

where V_m = molar volume, $2y$ = number of sodium per formula unit, and N_A = Avogadro's number. The strain contribution to the activation energy is given by [50]

$$\Delta E_S = \pi G(x)\frac{\lambda}{2}\left(r_{Na} - r_D\right)^2 \tag{12}$$

where the shear modulus G may be estimated by Gilman's expression [51]

$$G(x) = \frac{3e^2}{4\pi\left(r_{Na} + r_S\right)\alpha} \tag{13}$$

$$\alpha = \frac{3\varepsilon_0\left(\varepsilon_\infty - 1\right)}{\varepsilon_\infty + 2}\frac{M}{\rho N_A} \tag{14}$$

Here $r_D =$ doorway radius, the opening size available to the sodium ion for motion through the glass; $\rho =$ mass density; $\varepsilon_0 =$ permittivity of free space; $M =$ molar mass.

The values used were: $r_{Na} = 1.02$ Å, $r_S = 1.84$ Å (Ref.[52]), and $Z_{Na} = +1$, $Z_S = -1$, $\varepsilon_\infty\, r_D$, M, ρ, V_m [37,39].

Fig. 11 shows the results of the model compared with ΔE_{act} determined from NMR and conductivity measurements.

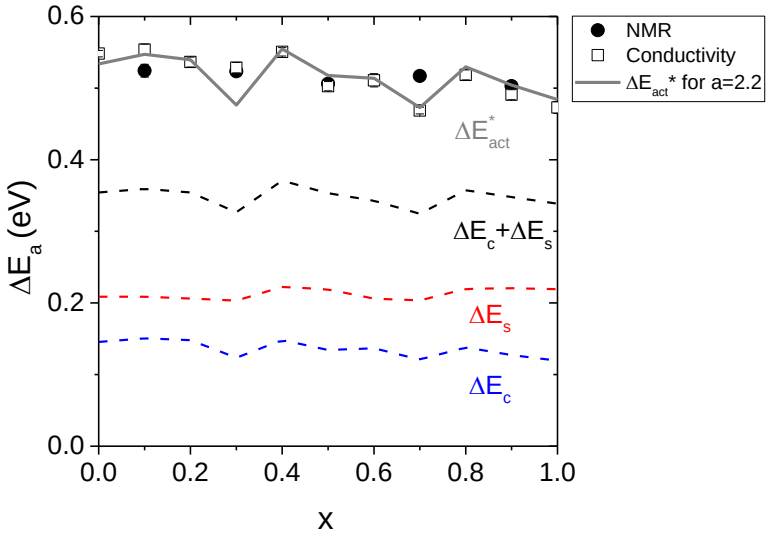

FIGURE 11. ^{23}Na energy barriers ΔE^*_{act} for $0.67Na_2S+0.33[xSiS_2+(1\text{-}x)PS_{5/2}]$ glass determined using sodium NMR measurements from this investigation, conductivity measurements reported in Ref.[37], and the Anderson-Stuart model as calculated from Eqn. (16), where a is an adjustable multiplicative constant for the Coulombic energy.

The sum of the Coulomb and strain energy terms $\Delta E_{act} = \Delta E_C + \Delta E_S$ is significantly and systematically lower than the experimental values across the entire composition range. This is not surprising, since the model includes only a single sodium-sulfur interaction. A simple but revised model may be obtained by adjusting the Coulombic interaction by a

multiplicative constant *a*, which here plays a role similar to the Madelung constant found in crystalline systems [30]

$$\Delta E_C^* = aE_C \tag{15}$$

The adjusted total activation energy is

$$\Delta E_{act}^* = \Delta E_C^* + \Delta E_S \tag{16}$$

Figure 11 shows ΔE_{act}^* calculated for *a*=2.2±0.1, and using this factor for all sample compositions one finds that ΔE_{act}^* matches the data within three standard deviations for most data points. We note that the value for the Madelung constant found here is similar to the value reported in the y=0.5 germanium analog system, which uses a Ge-based glass former rather than the Si-based former used here [30]. This may be interpreted then as the correction factor for incorporating the full set of sodium-sulfur interaction of the glass originally ignored in the simple model of Fig. 10.

Figure 12 (a) compares ΔE_{act}^* with experimental ΔE_{act} values obtained by DC conductivity and NMR for the y=0.67 sample.

FIGURE 12. (a) Detail of ^{23}Na energy barriers ΔE^*_{act} for $0.67Na_2S+0.33[xSiS_2+(1-x)PS_{5/2}]$ glass using sodium NMR measurements from this investigation, conductivity measurements reported in Ref.[37], and the Anderson-Stuart model as calculated from Eqn. (16). (b) Ratios of $\frac{\lambda_x}{\lambda_{x=0}}$, $\frac{\varepsilon_{\infty x}}{\varepsilon_{\infty x=0}}$, obtained from experimental values, and ratio $\frac{\Delta E^*_x}{\Delta E^*_{x=0}}$ based on calculated ΔE^*_{act} in (a).

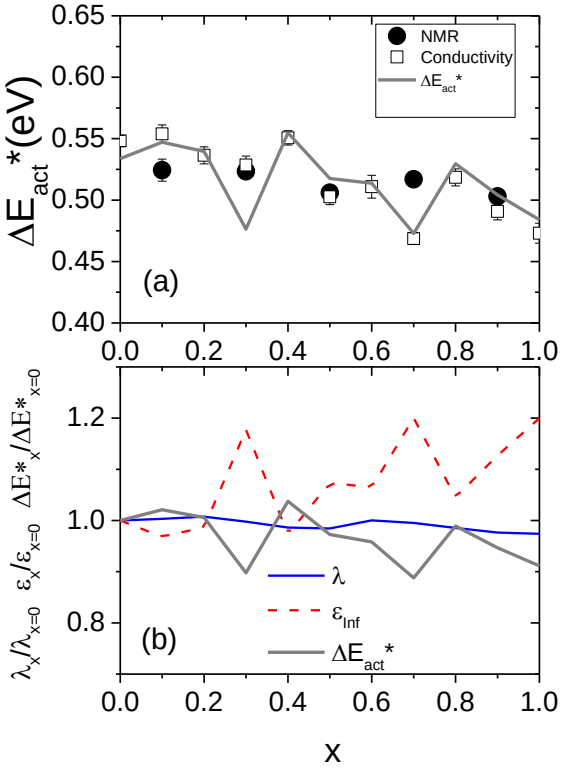

Note that ΔE^*_{act} is within three standard deviations for experimental data for all but one sample composition, x = 0.3. Taking the view that ΔE^*_{act} and Eqn. (16) model the experimental data reasonably well, Fig. 12(b) probes how variations in the only two experimental parameters of the model, λ and ε_∞, compare to variations in ΔE^*_{act}. Ignoring for the moment the values at x = 0.3, one sees that fluctuations in the dielectric constant ε_∞mirror the changes in ΔE^*_{act}, and are nearly 20 times larger than changes in λ over the

entire range of x. Thus, the energy barriers, and the conducting properties that result, are driven strongly by the dielectric properties of the glass.

C. Percolation model and the Na^+ ion conductivity

Figure 13 shows the composition dependence of the Na^+ ion DC conductivity values at 30 °C for the y=0.67 samples.

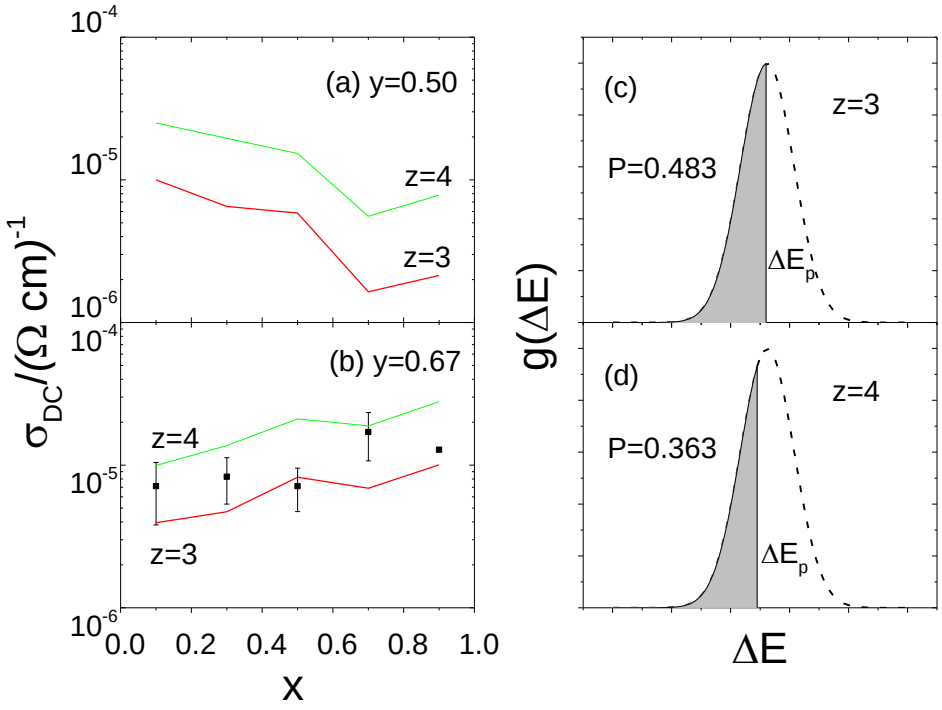

FIGURE 13. DC conductivity for $yNa_2S+(1-y)[xSiS_2+(1-x)PS_{5/2}]$ glass at 30 °C. The solid line represents values calculated based on NMR data and the percolation theory model as described in the text, and assuming a sodium coordination number of *z*=3 (red) and z=4 (green). (a) Values for y=0.50 sample. (b) Values for y=0.67 sample. The data points are experimental values taken from Ref.[37]. (c) A schematic Gaussian DAE for sodium coordination number z=3. The shaded area represents the fraction P of ions participating in conduction at the percolation threshold. (d) A similar plot for z=4.

These experimental values were taken from Ref.[37] for the y = 0.67 samples. So far, the DC conductivity for the y = 0.5 series of glasses have not been measured, but will be reported on in future publications in this series.

The DC conductivity may be estimated from NMR data using percolation theory [21,23,27,53]. In this model, the glassy nature of the material provides a variety of pathways for the sodium to move, each with a different ΔE_{act} value, representing the relative difficulty of taking a given pathway. Mobile charge percolates through the network, and below a critical fraction P of pathways, known as the critical percolation threshold, the DC conductivity is zero [54]. The critical threshold is related to the number of sodium nearest neighbor sites z by the empirically determined relation for regular 3-dimensional lattices [54]

$$P = \frac{1.45}{z}. \tag{17}$$

This relationship is a near-invariant for percolation [54], and indicates that at the percolation threshold the average cation site sees approximately $zP \approx 1.5$ unblocked pathways. In this model, pathways above activation energy threshold ΔE_p are considered blocked, and this threshold satifies [21]

$$P = \int_0^{\Delta E_P} g\left(\Delta E\right) d\Delta E. \tag{18}$$

Thus, for a given z, one may determine P, and from the NMR-determined distribution g(ΔE), ΔE_p may be found. For this study, z is taken as a free parameter, and Fig. 13 (c) and (d)

show schematic DAE and ΔE_p for z=3 and z=4. The effective time between cation hops between sites is time average [21,23]

$$\tau_{avg}(T) = \frac{1}{zP}\int_0^{\Delta E_p} \tau(\Delta E)\, g(\Delta E)\, d\Delta E \tag{19}$$

and is interpreted as the correlation time for the ions determining the DC current. The DC conductivity for uncorrelated sodium jumps assuming equal jump distances λ and a sodium concentration C is given by [21,23]

$$\sigma_{DC} = \frac{CPe^2\lambda^2}{6k_B T\tau_{avg}} \tag{20}$$

Figure 13(b) shows σ_{DC} determined using the percolation theory model for the y = 0.67 sample, for z=3 and z=4 (solid lines). Comparison with experimental values shows general agreement with z in this range, but the scatter in the data does not allow clear determination of a specific value. From percolation theory, one generally expects that the activation energy found from NMR will be higher than that obtained by σ_{DC}measurements. This is due to the fact that only the lower energy pathways are explored for σ_{DC}, whereas NMR simultaneously probes the dynamics of all sodium ions, whether they jump or not. Fig. 12 (a) shows that for the five compositions for which ΔE_{act} data exist for both methods, three yielded ΔE_{act} values that were within 3 standard deviations of one another. One possible explanation may be seen from Fig. 13 (c) and (d). From Eqns. (17) and (18) one finds that for z=3, $\Delta E_p = \Delta E_{act} - 0.042\sigma_E$ where ΔE_{act} and σ_E are the mean and standard deviation of the NMR-determined activation energy distribution. Taking ΔE_p as an estimate

of the expected average activation energy from DC conductivity, this model predicts a smaller ΔE_p. As z gets larger, the difference between NMR- and DC conductivity-determined values becomes more pronounced. The difference is within 1 error bar. For z=4 the same analysis yields $\Delta E_p = \Delta E_{act} - 0.35\sigma_E$ and the difference is within 3 error bars. The percolation model therefore accounts for the DC conductivity values and the small differences between the NMR- and conducitivity determined activation energies, and is consistent with z=3-4.

In Fig. 13(a) we show the same model applied to the y = 0.50 system, and assume a similar coordianation of the cation. The solid lines indicate calculated DC conductivity values for z=3 and z=4 based on the NMR-determined DAE, and indicate a downward trend with increasing x. This is consistent with a Ge analog of this system for which z=4 [30]. The estimates here represent the first determination of conductivity for these samples.

D. Length scales from M_2 measurements

The length scale of the sodium-sodium separation was probed in two ways. From Eqn. (11), the molar volume V_m data and the stoichiometry of the glass, one can calculate a separation distance that reflects an average cation separation across the sample. A more refined method is obtained from M_2, which measures the strength of the homonuclear ^{23}Na magnetic dipole-dipole interaction. Assuming all the radii of the sodium coordination shells scale by the same factor α so that $r_{ij}^{'} = \alpha r_{ij}$, Eqn. (4) gives

$$\frac{r'}{r} = \left(\frac{M_2'}{M_2} \right)^{-1/6} \tag{21}$$

Figure 14 shows the ^{23}Na second moments M_2 for y = 0.50 and 0.67 glass series across the SiS_2 composition range x.

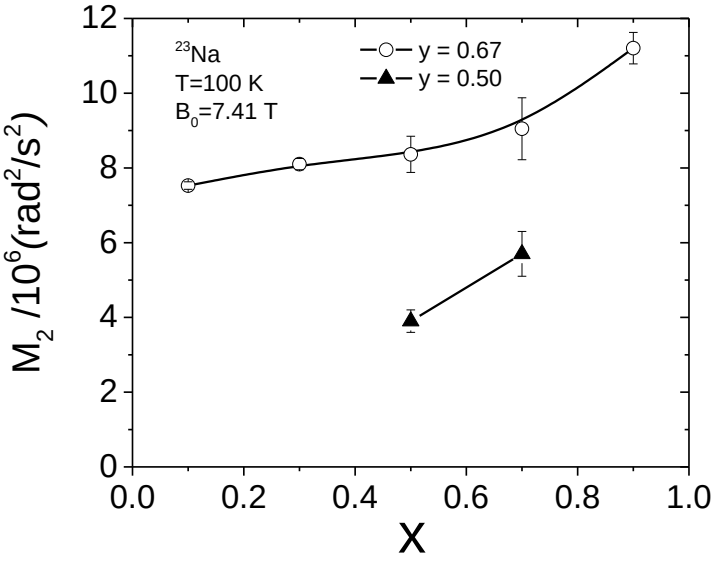

FIGURE 14. Second moment of ^{23}Na central line for $yNa_2S+(1-y)[xSiS_2+(1-x)PS_{5/2}]$ glasses for *y* = 0.50, 0.67. Solid lines are guides for the eye.

Both data sets suggest a trend to larger M_2 with larger x, indicating the sodium-sodium distances are decreasing. Figure 15 shows the ratio of sodium-sodium distances estimated using these two methods.

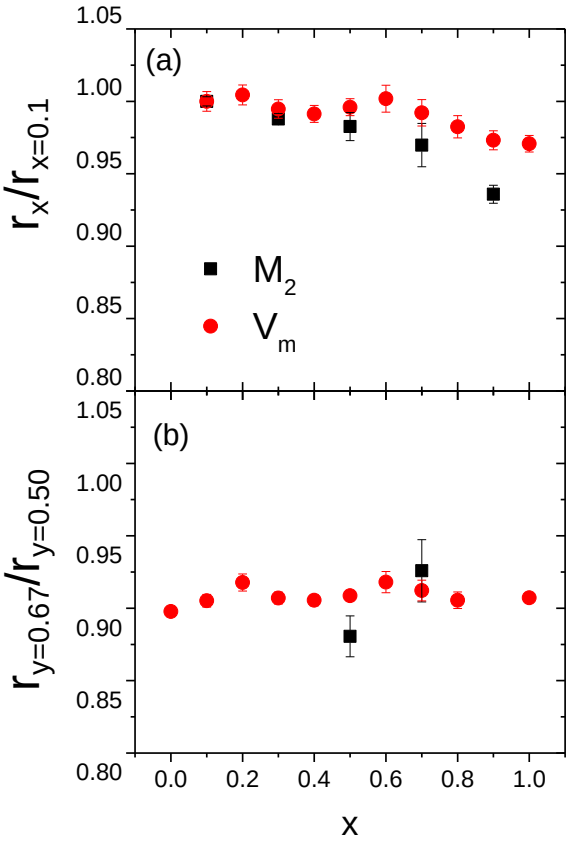

FIGURE 15. Ratios of sodium-sodium distances for $yNa_2S+(1-y)[xSiS_2+(1-x)PS_{5/2}]$ glasses. The values are estimated two ways: using the M_2 values of Fig. 14 and ratio calculated from Eqn. (21), and using molar volume data and Eqn. (11). (a) For y=0.67, the ratio $r_x / r_{x=0.1}$ was calculated, the ratio relative to the sodium-sodium distance value for the x=0.1 sample. (b) The ratio $r_{y=0.67} / r_{y=0.50}$ was calculated for each x value, comparing sodium-sodium distance values for the 0.67 sample to the 0.50 sample.

Figure 15 (a) plots $r_x / r_{x=0.1}$ for the y = 0.67 series of glasses as a function of x, comparing distances for each composition x to that obtained for the x=0.1 sample. Both M_2 and V_m methods show a trend to shorter sodium-sodium distances with increasing x. At x = 0.9, the M_2 data reveal that the sodium-sodium distance is smaller than that at x = 0.1 by (6.5 ± 0.5) %, as compared with the V_m method which shows a reduction by (2.7 ± 0.7) %. Since the distance obtain from V_m represents an average over the entire sample, and that from M_2

from a probe of local sodium interactions, the discrepancy between the two is not surprising. Figure 15 (b) shows $r_{0.67} / r_{0.50}$ as a function of x, comparing the y = 0.67 with the y = 0.50 series of sodium-sodium distances for each composition x. At each x, the increased sodium concentration should result in a change in sodium distance. From the graph, one sees that the volumetric data show a nearly constant ratio of $\frac{r_{0.67}}{r_{0.50}}$ = (91 ± 1)% when taken across all compositions x. The smaller $r_{y=0.67}$ distances are consistent with the higher sodium concentration y. There is no significant difference between this value and those obtained from M_2 for the data available, suggesting that volume changes appear to account for the changes in sodium-sodium distances with changing y.

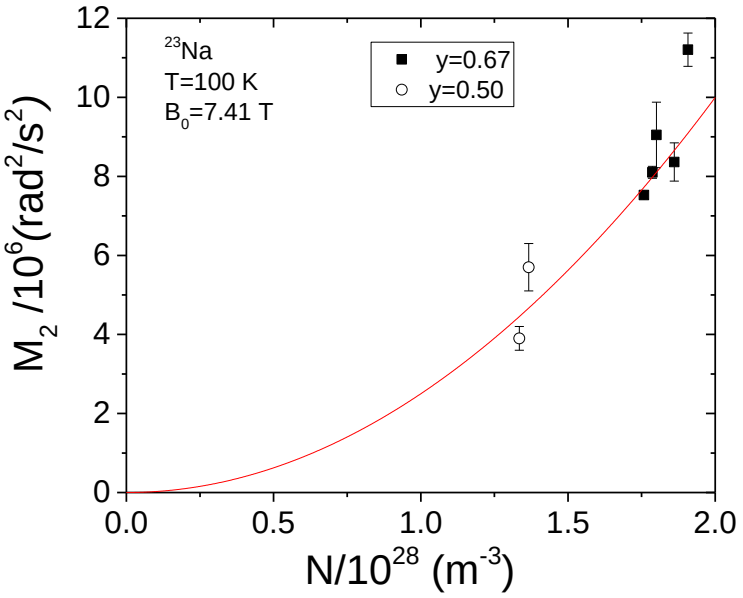

FIGURE 16. Second moment of ^{23}Na central line versus sodium number density for $yNa_2S+(1-y)[xSiS_2+(1-x)PS_{5/2}]$ glasses, y = 0.50, 0.67. Solid line is a fit proportional to N^2.

Fig. 16 shows M_2 versus sodium number density N. If the increase in number density is associated with a homogeneous change in the Na-Na coordination shells $r_{ij}^{'} = \alpha r_{ij}$ thoughout the structure, one expects from Eqn. (4) that $M_2 \propto N^2$ [41]. A fit proportional to N^2 in Fig. 16 shows that the data is consistent with a homogeneous distribution. Only the y=0.67, x=0.9 value shows a significant deviation above this line, suggesting that at higher concentrations in this system there may be a tendency for sodium aggregation.

Conclusions

We performed a ^{23}Na NMR study of the $yNa_2S + (1-y)[xSiS_2+(1-x)PS_{5/2}]$ for y = 0.5 and 0.67, and x = 0.1, 0.3, 0.5, 0.7, and 0.9. Using ^{23}Na central line widths as a function of temperature, and ^{23}Na central line relaxation as a function of temperature, a Gaussian DAEs was found consistent with experimental data, and mean barrier values were extracted. Though no pronounced MGFE was observed within experimental error for either sample, for increasing SiS_2 concentration *x* the mean barrier height, ΔE_{act}, decreased across the composition range for the *y* = 0.67 series, and an increased for the *y* = 0.50 series. The DC conductivity values calculated using NMR-derived correlation times, a sodium coordination number z = 3, and energy cutoff determined from the critical percolation threshold, were in agreement with experimental values in the y = 0.67 series of glasses. Using the same model, values were calculated for the y = 0.50 sample, and these revealed a decreasing conductivity as x increased. Energy barriers to sodium motion were analyzed using the Anderson-Stuart model for the y = 0.67 series, and this analysis suggested that the energy barriers as a function of composition are strongly influenced by the dielectric constant of these materials. Sodium clustering becomes more pronounced with increasing *x* in the y =

0.67 sample, as seen by NMR second moment measurements that show sodium-sodium separation distances decreasing by 6.5% across the full composition range sample.

Acknowledgments

Thanks to S. Tani, S. A. Thomas, M. Foley, G. Buehler, and A. Eshete for assisting with numerous calculations, and B. Curtis for helping with sample preparation. M. Storek is thanked for graciously providing software for the simultaneous fits described in the text. Funding for this research was provided in part by the NSF through grants DMR 0710564 and 1304977. DW was supported in part by an ISU NSF AGEP Fellowship. In addition, support came from the U.S. Department of Energy, Office of Basic Energy Sciences, Division of Materials Sciences and Engineering. Ames Laboratory is operated for the U.S. Department of Energy by Iowa State University under Contract No. DEAC02-07CH11358.

References

[1] K.L. Ngai, Relaxation and Diffusion in Complex Systems, Springer New York, 2011.

[2] V. Palomares, P. Serras, I. Villaluenga, K.B. Hueso, J. Carretero-Gonzalez, T. Rojo, Na-ion batteries, recent advances and present challenges to become low cost energy storage systems, Energy Environ. Sci. 5 (2012) 5884-5901.

[3] M.D. Slater, D. Kim, E. Lee, C.S. Johnson, Sodium-Ion Batteries, Advanced Functional Materials. 23 (2013) 947-958.

[4] H. Pan, Y. Hu, L. Chen, Room-temperature stationary sodium-ion batteries for large-scale electric energy storage, Energy Environ. Sci. 6 (2013) 2338-2360.

[5] M. Nagao, A. Hayashi, M. Tatsumisago, T. Kanetsuku, T. Tsuda, S. Kuwabata, In situ SEM study of a lithium deposition and dissolution mechanism in a bulk-type solid-state cell with a Li_2S-P_2S_5 solid electrolyte, Phys. Chem. Chem. Phys. 15 (2013) 18600-18606.

[6] A. Hayashi, S. Hama, T. Minami, M. Tatsumisago, Formation of superionic crystals from mechanically milled Li_2S–P_2S_5 glasses, Electrochemistry Communications. 5 (2003) 111-114.

[7] M. Schuch, C.R. Mueller, P. Maass, S.W. Martin, Mixed Barrier Model for the Mixed Glass Former Effect in Ion Conducting Glasses, Phys. Rev. Lett. 102 (2009) 145902.

[8] R. Christensen, G. Olson, S.W. Martin, Structural Studies of Mixed Glass Former $0.35Na_2O + 0.65[xB_2O_3 + (1 - x)P_2O_5]$ Glasses by Raman and ^{11}B and ^{31}P Magic Angle Spinning Nuclear Magnetic Resonance Spectroscopies, J Phys Chem B. 117 (2013) 2169-2179.

[9] C. Bischoff, K. Schuller, S.P. Beckman, S.W. Martin, Non-Arrhenius Ionic Conductivities in Glasses due to a Distribution of Activation Energies, Phys. Rev. Lett. 109 (2012) 075901.

[10] M. Storek, M. Adjei-Acheamfour, R. Christensen, S.W. Martin, R. Boehmer, Positive and Negative Mixed Glass Former Effects in Sodium Borosilicate and Borophosphate Glasses Studied by ^{23}Na NMR, The Journal of Physical Chemistry B. 120 (2016) 4482-4495.

[11] D.E. Watson, S.W. Martin, Short range order characterization of the Na_2S+SiS_2 glass system using Raman, infrared and ^{29}Si magic angle spinning nuclear magnetic resonance spectroscopies, Journal of Non-Crystalline Solids. 471 (Supplement C) (2017) 39-50.

[12] R. Christensen, G. Olson, S.W. Martin, Ionic Conductivity of Mixed Glass Former $0.35Na_2O + 0.65[xB_2O_3 + (1 - x)P_2O_5]$ Glasses, J Phys Chem B. 117 (2013) 16577-16586.

[13] A. Abragam, Principles of Nuclear Magnetism, Clarendon Press, Oxford, 1989.

[14] C.P. Slichter, Principles of Magnetic Resonance, Springer-Verlag, New York, 1990.

[15] M.H. Levitt, Spin Dynamics : Basics of Nuclear Magnetic Resonance, 2nd ed., John Wiley & Sons, Chichester, England ; Hoboken, NJ, 2008.

[16] R. Böhmer, K.R. Jeffrey, M. Vogel, Solid-state Li NMR with applications to the translational dynamics in ion conductors, Progress in Nuclear Magnetic Resonance Spectroscopy. 50 (2007) 87-174.

[17] H. Eckert, Structural characterization of noncrystalline solids and glasses using solid state NMR, Prog Nucl Magn Reson Spectrosc. 24 (1992) 159-293.

[18] B. Gee, H. Eckert, 23Na nuclear magnetic resonance spin echo decay spectroscopy of sodium silicate glasses and crystalline model compounds, Solid State Nuclear Magnetic Resonance. 5 (1995) 113-122.

[19] K.H. Kim, D.R. Torgeson, F. Borsa, J.P. Cho, S.W. Martin, I. Svare, G. Majer, Evidence of complex ionic motion in $\chi Li_2S + (1 - \chi)B_2S_3$ glassy fast ionic conductors from ^{7}Li and ^{11}B NMR and ionic conductivity measurements, Journal of Non-Crystalline Solids. 211 (1997) 112-125.

[20] I. Svare, F. Borsa, D.R. Torgeson, S.W. Martin, Connection between NMR relaxation and electrical conductivity from distributions of activation energies of ionic motion in some fast-ion conductors, Journal of Non-Crystalline Solids. 172 (1994) 1300-1305.

[21] I. Svare, Conductivity and NMR relaxation from ionic motion in disordered glasses with distributions of barriers, Solid State Ionics. 125 (1999) 47-53.

[22] K.H. Kim, D.R. Torgeson, F. Borsa, J. Cho, S.W. Martin, I. Svare, Distribution of activation energies explains ionic motion in glassy fast ion conductors: ^{7}Li NMR spin-lattice relaxation and ionic conductivity in $xLi_2S + (1-x)GeS_2$, Solid State Ionics. 91 (1996) 7-19.

[23] I. Svare, F. Borsa, D.R. Torgeson, S.W. Martin, Correlation functions for ionic motion from NMR relaxation and electrical conductivity in the glassy fast-ion conductor $(Li_2S)_{0.56}(SiS_2)_{0.44}$, Phys.Rev.B. 48 (1993) 9336-9344.

[24] M. Storek, R. Böhmer, S.W. Martin, D. Larink, H. Eckert, NMR and conductivity studies of the mixed glass former effect in lithium borophosphate glasses, J. Chem. Phys. 137 (2012) 124507.

[25] J. Gabriel, O.V. Petrov, Y. Kim, S.W. Martin, M. Vogel, Lithium ion dynamics in $Li_2S+GeS_2+GeO_2$ glasses studied using ^{7}Li NMR field-cycling relaxometry and line-shape analysis, Solid State Nuclear Magnetic Resonance. 70 (2015) 53-62.

[26] F. Borsa, D.R. Torgeson, S.W. Martin, H.K. Patel, Relaxation and fluctuations in glassy fast-ion conductors: Wide-frequency-range NMR and conductivity measurements, Phys. Rev. B. 46 (1992) 795-800.

[27] I. Svare, S.W. Martin, F. Borsa, Stretched exponentials with T-dependent exponents from fixed distributions of energy barriers for relaxation times in fast-ion conductors, Phys. Rev. B. 61 (2000) 228-233.

[28] B. Meyer, F. Borsa, D.M. Martin, S.W. Martin, NMR spin-lattice relaxation and ionic conductivity in lithium thioborogermanate fast-ion-conducting glasses, Phys. Rev. B. 72 (2005) 144301.

[29] J. Cho, S.W. Martin, Structures and ionic conduction of $xNa_2S+(1-x)SiS_2$ glasses, Ceramic Transactions. 65 (1996) 85-99.

[30] S.W. Martin, C. Bischoff, K. Schuller, Composition Dependence of the Na+ Ion Conductivity in $0.5Na_2S + 0.5xGeS_2 + (1-x)PS_{5/2}$] Mixed Glass Former Glasses: A Structural Interpretation of a Negative Mixed Glass Former Effect, J Phys Chem B. 119 (2015) 15738-15751.

[31] D. Larink, H. Eckert, S.W. Martin, Structure and Ionic Conductivity in the Mixed-Network Former Chalcogenide Glass System $[Na_2S]_{2/3}[(B_2S_3)_x(P_2S_5)_{1-x}]_{1/3}$, J. Phys. Chem. C. 116 (2012) 22698-22710.

[32] I. Seo, S.W. Martin, Preparation and Characterization of Fast Ion Conducting Lithium Thio-Germanate Thin-Films Grown by RF Magnetron Sputtering, ECS Transactions. 28 (2010) 287-297.

[33] W. Yao, S.W. Martin, Ionic conductivity of glasses in the $MI+M_2S+(0.1Ga_2S_3+0.9GeS_2)$ system (M=Li, Na, K and Cs), Solid State Ionics. 178 (2008) 1777-1784.

[34] J. Saienga, S.W. Martin, The comparative structure, properties, and ionic conductivity of $LiI+Li_2S+GeS_2$ glasses doped with Ga_2S_3 and La_2S_3, Journal of Non-Crystalline Solids. 354 (2008) 1475-1486.

[35] Y. Kim, J. Saienga, S.W. Martin, Anomalous Ionic Conductivity Increase in $Li_2S + GeS_2 + GeO_2$ Glasses, J Phys Chem B. 110 (2006) 16318-16325.

[36] D.E. Watson, S.W. Martin, Structural Characterization of the Short-Range Order in High Alkali Content Sodium Thiosilicophosphate Glasses, Inorg. Chem. 57 (2018) 72-81.

[37] D.E. Watson, Mixed glass former effect of $0.5Na_2S+0.5[xSiS_2+(1-x)PS_{5/2}]$ and $0.67Na_2S+0.33[xSiS_2+(1-x)PS_{5/2}]$ glass systems, Ph. D. Dissertation, Iowa State University. (2017).

[38] O.L. Anderson, D.A. Stuart, Calculation of Activation Energy of Ionic Conductivity in Silica Glasses by Classical Methods, J Am Ceram Soc. 37 (1954) 573-580.

[39] D.E. Watson, S.W. Martin, Composition Dependence of the Glass-Transition Temperature and Molar Volume in Sodium Thiosilicophosphate Glasses: A Structural Interpretation Using a Real Solution Model, J Phys Chem B. 122 (2018) 10637-10646.

[40] E. Fukushima, S.B.W. Roeder, Experimental Pulse NMR: A Nuts and Bolts Approach, Addison-Wesely Publishing Company, Inc., Reading, Massachusetts, 1981.

[41] H. Eckert, Short and Medium Range Order in Ion-Conducting Glasses Studied by Modern Solid State NMR Techniques, Zeitschrift fuer Physikalische Chemie. 224 (2010) 1591.

[42] M. H. Cohen, F. Reif, Quadrupole Effects in Nuclear Magnetic Resonance Studies of Solids, in: Solid State Physics, in: D.T. F. Seitz (Ed.), Academic Press, New York, 1957, pp. 321-438.

[43] A. Narath, Nuclear Spin-Lattice Relaxation in Hexagonal Transition Metals: Titanium, Phys.Rev. 162 (1967) 320-332.

[44] R. Mossadegh, C.T. Moynihan, A.J. Bruce, M.G. Drexhage, DSC studies of melting behavior of heavy metal fluoride glass compositions, Materials Research Bulletin. 22 (1987) 593-600.

[45] J. Haase, E. Oldfield, Spin-Echo Behavior of Nonintegral-Spin Quadrupolar Nuclei in Inorganic Solids, J. Magn. Reson. Series A. 101 (1993) 30.

[46] T.-. Phua, B.J. Beaudry, D.T. Peterson, D.R. Torgeson, R.G. Barnes, M. Belhoul, G.A. Styles, E.F.W. Seymour, Paramagnetic impurity effects in NMR determinations of hydrogen diffusion and electronic structure in metal hydrides. ${\mathrm{Gd}}^{3+}$ in Y${\mathrm{H}}_{2}$ and La${\mathrm{H}}_{2.25}$, Phys. Rev. B. 28 (1983) 6227-6250.

[47] N.A. Sergeev, M. Paczwa, M. Olszewski, A.M. Panich, **^{23}Na and ^{27}Al NMR Study of Structure and Dynamics in Mordenite**, Appl. Magn. Reson. 48 (2017) 115.

[48] A.M. Panich, N.A. Sergeev, Nuclear spin-lattice relaxation in carbon nanostructures, Physica B: Condensed Matter. 405 (2010) 2034-2038.

[49] J.L. Bjorkstam, J. Listerud, M. Villa, C.I. Massara, Motional narrowing of a gaussian NMR line, Journal of Magnetic Resonance (1969). 65 (1985) 383-394.

[50] D. McElfresh, D.G. Howitt, Activation Enthalpy for Diffusion in Glass, J Am Ceram Soc. 69 (1986) C-237-C-238.

[51] J.J. Gilman, Chemistry and Physics of Mechanical Hardness, John Wiley and Sons, New York, 2009.

[52] R.D. Shannon, Revised effective ionic radii and systematic studies of interatomic distances in halides and chalcogenides, Acta Cryst. A32 (1976) 751-767.

[53] S.W. Martin, F. Borsa, I. Svare, Proc. Electrochem. Soc. 2000-32 (2001) 66.

[54] R. Zallen, The Physics of Amorphous Solids, John Wiley and Sons, Weinheim, Federal Republic of Germany, 2004.